ARTICLE

Multistep Lithiation of Tin Sulfide: An Investigation Using *in Situ* Electron Microscopy

Sooyeon Hwang,[†] Zhenpeng Yao,[‡] Lei Zhang,[§] Maosen Fu,[ǁ,†] Kai He,[‡] Liqiang Mai,[§] Chris Wolverton,[‡] and Dong Su*,[†]

[†]Center for Functional Nanomaterials, Brookhaven National Laboratory, Upton, New York 11973, United States

[‡]Department of Materials Science and Engineering, Northwestern University, Evanston, Illinois 60208, United States
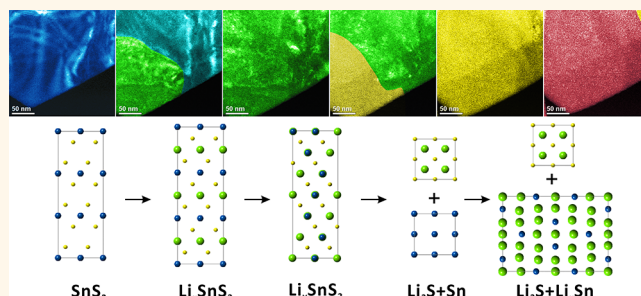
[§]State Key Laboratory of Advanced Technology for Materials Synthesis and Processing, Wuhan University of Technology, Wuhan 430070, P. R. China

[ǁ]Shanxi Materials Analysis and Research Center, School of Materials Science and Engineering, Northwestern Polytechnical University, Xi'an 710000, P. R. China

ⓢ *Supporting Information*

ABSTRACT: Two-dimensional (2D) metal sulfides have been widely explored as promising electrodes for lithium-ion batteries since their two-dimensional layered structure allows lithium ions to intercalate between layers. For tin disulfide, the lithiation process proceeds *via* a sequence of three different types of reactions: intercalation, conversion, and alloying, but the full scenario of reaction dynamics remains nebulous. Here, we investigate the dynamical process of the multistep reactions using *in situ* electron microscopy and discover the formation of an intermediate rock-salt phase with the disordering of Li and Sn cations after

initial 2D intercalation. The disordered cations occupy all the octahedral sites and block the channels for intercalation, which alter the reaction pathways during further lithiation. Our first-principles calculations of the nonequilibrium lithiation of SnS_2 corroborate the energetic preference of the disordered rock-salt structure over known layered polymorphs. The *in situ* observations and calculations suggest a two-phase reaction nature for intercalation, disordering, and following conversion reactions. In addition, *in situ* delithiation observation confirms that the alloying reaction is reversible, while the conversion reaction is not, which is consistent with the *ex situ* analysis. This work reveals the full lithiation characteristic of SnS_2 and sheds light on the understanding of complex multistep reactions in 2D materials.

KEYWORDS: lithium-ion batteries, in situ transmission electron microscopy, tin disulfide, multistep lithiation, density functional theory

Current widespread usage of lithium-ion batteries (LIBs) in a number of electronic devices has been realized by using intercalation-type of electrode materials, such as carbonaceous materials and lithium transition-metal oxides.[1,2] As lithium ions can be inserted into and extracted from empty spaces inside electrode materials, the original structures of host compounds are well maintained during operation, which improves reversibility and long-term stability. Despite their success in market, these kinds of materials have intrinsic limitations on energy density because of the limited number of vacant sites inside host compounds. Conversion-type nanosized materials (metal oxides, sulfides, fluorides, *etc.*)[3−8] and alloying-type materials (Si, Sb, Ge, Sn, *etc.*)[9,10] can be attractive alternatives which offer much higher energy density for LIBs. However, these types of materials also have problematic issues, for example, volume expansion, mechanical integrity, reversibility, and long-term stability. The mechanism by which electrode materials store Li ions governs the characteristics of battery cells; therefore,

thorough understanding of the lithiation process is of importance for improving the figures-of-merits of electrode materials.
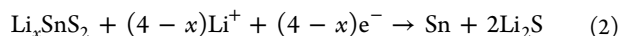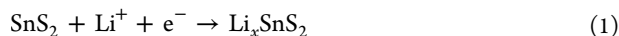
Some metal chalcogenides which adopt a two-dimensional (2D) layered structure have exhibited intriguing lithium insertion reactions. Since adjacent metal sulfur layers are bonded by the relatively weak van der Waals force,[11,12] Li-ions can be intercalated between these adjacent metal−sulfur layers. This characteristic has made metal chalcogenides draw an intensive amount of attention as electrode materials in late 1970s.[13,14] Despite the similar 2D structure across many chalcogenides,[11,13,15,16] different metal sulfides may have distinct lithiation reaction mechanisms. In case of MoS_2, the intercalation of Li ions is accompanied by a Mo coordination change from trigonal prismatic to

octahedral,[17] followed by a conversion process from Li_xMoS_2 to Li_2S and Mo.[18] For copper sulfides (CuS, Cu_2S), after the intercalation reaction, an extrusion (displacement) reaction takes place rather than the conversion reaction.[19−21] Among these 2D layered chalcogenides, SnS_2 has an interesting and complicated reaction nature with lithium, which featured with consequently connected three different types of reactions: intercalation, conversion, and alloying:[22,23]

$$SnS_2 + Li^+ + e^- \rightarrow Li_xSnS_2 \tag{1}$$

$$Li_xSnS_2 + (4 - x)Li^+ + (4 - x)e^- \rightarrow Sn + 2Li_2S \tag{2}$$

$$Sn + 4.4Li \leftrightarrow Li_{4.4}Sn \tag{3}$$

It is believed that the conversion reaction is not reversible which largely instigates a low Coulombic efficiency during the first cycle.[24−26] Thus, only 645 mAh/g originated from alloying reaction is reversible, while the theoretical capacity for whole reaction is up to 1231 mAh/g. As electrochemical performance is highly dependent on how these reactions proceed, for example, the reaction pathways, intermediate phases involving this complicated reaction process,[22,23,27,28] real-time investigation is necessary to improve figure-of-merits of electrode materials. A couple of studies performed *in situ* electron microscopy work of SnS_2: Gao et al.[27] studied the intercalation and deintercalation processes, and Yin et al.[28] reported formation of self-assembled composite framework after the first discharge process. However, up to now, the microscopic investigation on the whole different types of lithiation reactions still lacks for SnS_2, and insights regarding a full scenario of reaction dynamics remain elusive.

Herein, we perform a mechanistic study on the lithiation and delithiation processes of tin disulfide using *in situ* transmission electron microscopy (TEM) in combination with first-principles calculations. Our *in situ* selected area electron diffraction (SAED) and scanning TEM (STEM) results elucidate four sequential reaction steps during the lithiation of SnS_2. A disordering transition with the formation of rock-salt phase is discovered after initial intercalation. The rearrangement of cations happens with Li and Sn equally occupying the octahedral sites and completely changes the structure of the layered compound, making the Li-intercalation impossible. After the disordering transition, further lithiation will prompt a conversion reaction with the collapse of crystal lattice. We note that the electron beam may induce phase transition in the electrode materials for batteries.[29] To avoid that issue, we here performed the *in situ* STEM imaging at a dose rate around 0.3 pA/cm². In addition, DFT calculations are conducted to explore a variety of possible lithiation reaction pathways of SnS_2 and identify the ground-state reaction path, which validates the experimental observations. Precise real-time analysis performed here reveals full reaction natures of tin sulfides which cannot be acquired by post-mortem studies.

RESULTS AND DISCUSSION

Figure 1a−c shows scanning electron microscopy (SEM), high angle annular dark-field (HAADF)-scanning transmission electron microscopy (STEM), and high-resolution transmission electron microscopy (HRTEM) images of flower-like tin disulfide (SnS_2) samples studied in this work. Micron-sized flower samples are composed of pile-up of thin sheets. Figure S1a,c presents an X-ray diffraction pattern and HRTEM image along the [001] zone axis of SnS_2, indicating a 2H structure of space group $P\bar{3}m1$.
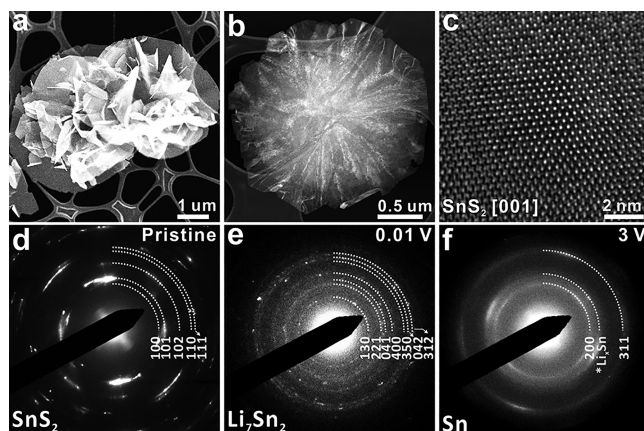

Figure 1. Pristine SnS_2 sample images acquired by (a) SEM, (b) HAADF, and (c) HRTEM. Diffraction patterns of SnS_2 at (d) pristine, (e) discharged to 0.01 V, and (f) charged to 3.0 V states, respectively.

STEM-electron energy loss spectroscopy (EELS) elemental maps in Figure S1b demonstrate the uniform distribution of Sn and S in SnS_2. The electrochemical activity of SnS_2 was examined in a coin cell, as shown in Figure S2. SAED patterns at pristine, discharged (0.01 V), and charged (3 V) states (Figure 1d−f, respectively) demonstrate that lithiation of SnS_2 results in formations of Li−Sn alloy phase, Li_7Sn_2, and removal of lithium ions leads to dealloying of Li−Sn instead of structural recovery of SnS_2. This is consistent with the previous reports.[22,25,30]

Real-time structural evolutions of SnS_2 during the lithium insertion were examined with both *in situ* electron diffraction and *in situ* imaging. We took advantage of a dry-format electrochemical cell setup.[31−34] We used Li/Li_2O on STM tip as the counter electrode/solid electrolyte and SnS_2 on lacey carbon Cu TEM grid as the active electrode for *in situ* experiments. Figure 2a presents radial intensity profiles as a function of reaction time produced from real-time SAEDs. The details of the data processing can be found in Figure S3. Raw video and SAED patterns are presented in Movie S1 and Figure S4, respectively. When lithium ions are introduced to SnS_2, the phase transitions can be determined by the modifications in radial intensity profiles (peak shift, disappearance or appearance of peaks). The radial intensity profile and corresponding diffraction patterns with false colors under each reaction are shown in Figure 2b,d, respectively. Instead of the three step reactions mentioned above, we have found four steps of lithiation processes of SnS_2: intercalation (0−288.4 s), disordering (~810.2 s), conversion (~1730.3 s), and alloying (1730.3 s to end). During the incipient stage of lithium insertion, we only observed the shrinkage and slight broadness of the diffraction profiles (261 s in Figure 2b), which mainly results from the expansion of unit cell (1.3% for a, 6.5% for c direction at the end of intercalation), correlating the phase transition from layered SnS_2 structure to layered Li_xSnS_2 structure. At this stage, lithium ions are introduced to octahedral sites between sulfur layers, while the 2D layered structure is preserved. Considering that lattice parameters of SnS_2 ($P\bar{3}m1$) and $LiSnS_2$ ($P\bar{3}m1$) are a = 3.638 Å, c = 5.88 Å (ICSD collection code 100610) and a = 3.67 Å, c = 7.9 Å (ICSD collection code 23451) in the hexagonal unit cell, insertion of one lithium ion per one SnS_2 chemical formula may induce 0.88% and 34.35% of lattice expansion in a and c directions, respectively. Thus, during first stage of reaction, intercalation of SnS_2 to Li_xSnS_2 would occur within a range of $x < 1$.
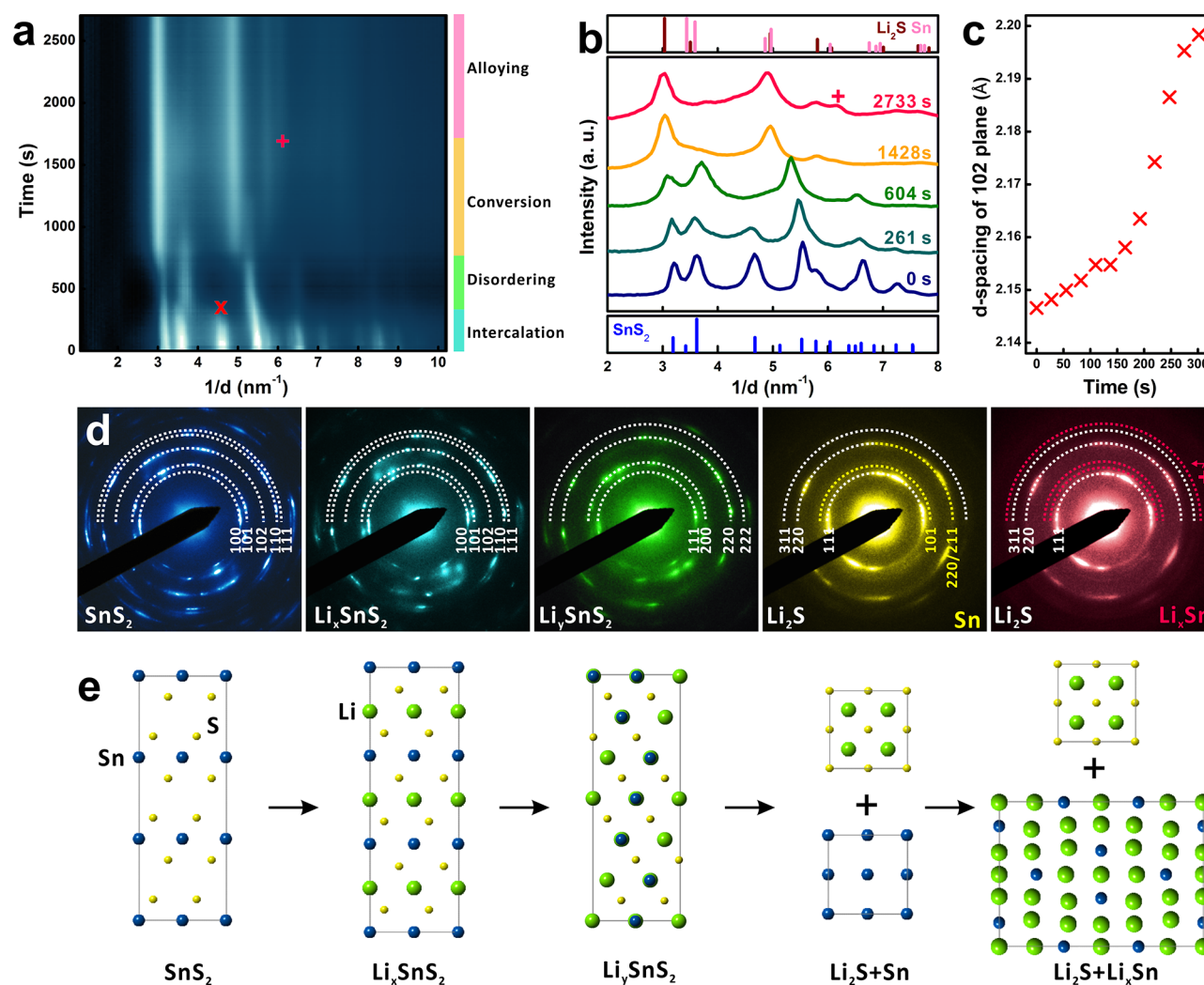
Figure 2. *In situ* SAED patterns of SnS_2 during lithiation. (a) Electron diffraction intensity profile as a function of reaction time during lithiation of SnS_2. X indicates a 102 diffraction peak, and + denotes the Li–Sn alloy phase. (b) Radial intensity profiles of diffraction patterns at certain times. (c) Changes in *d*-spacing of 102 plane during intercalation. (d) Diffraction patterns correspond to intensity profiles at (b). (e) Atomic models representing phase evolution during lithiation.

While the radial intensity profile at Figure 2a was generated with an averaged diffraction information from the selected area, Figure S5 exhibits changes in diffraction spots from a single SnS_2 sheet during intercalation. Clear splitting of $1\bar{2}1$ diffraction spot is observed, which can be attributed to a two-phase reaction nature as suggested in a previous report.[31] It is noteworthy that our *in situ* SAED patterns could track the subtle changes in *d*-spacing during the intercalation. Figure 2c presents the changes in *d*-spacing of 102 plane during intercalation reaction. In the case of *ex situ* SAED patterns recorded by CCD camera, we could have distortions and errors originating from recording system each time, which degrades the accuracy in determination of *d*-spacing. For our *in situ* electron diffraction, the instrumental error was consistent while taking videos; thus, the accuracy can be largely improved by measuring the relative shift of diffraction spots/rings. In addition, we use a subpixel fitting technique to fit the experimental data with a Voigt function (Figure S6),[35−37] providing a resolution of 0.0016 Å.

When additional lithium ions were inserted, the Li_xSnS_2 with layered structure was observed to transform to a Li_ySnS_2 having a face-centered cubic (FCC) structure evidenced by the characteristic FCC diffraction rings (Figures 2a and 604 s in Figure 2b).

With further simulation of electron diffraction (Figure S7), we deduced that Li_ySnS_2 has a disordered rock-salt structure. More information is available in the following calculation part and the Supporting Information. From 2D layered structure to rock-salt structure, two kinds of structural distortion are prompted: (1) The change in stacking sequence of each Sn–S layer is changing from A–A to A–B–C and (2) the disordering of Li and Sn ions along ⟨001⟩ zone axis of SnS_2 (which is identical to the ⟨111⟩ zone axis of rock-salt), resulting from the cation mixing. It is observed that further insertion of lithium ions triggers the conversion reaction. We could notice the emergence of diffraction rings from Li_2S and Sn (1428 s in Figure 2b), indicating the Li_ySnS_2 structure is decomposing. Further lithiation brings about additional diffraction rings, for example, the peak marked with "+" in Figure 2a,b,d, while the rings from Li_2S still are being presented. We believe this additional ring is the result of an alloying reaction between Sn metal and Li. We did not observe any strong reflections from the alloying phases which suggests the alloying reactions happened locally and no large crystals formed during our observation. The atomic models of these four step reactions are shown in Figure 2e.

The phase evolution of SnS_2 during lithiation was also investigated in real space with a STEM imaging technique, as presented in Figure 3. We performed STEM imaging videos at low
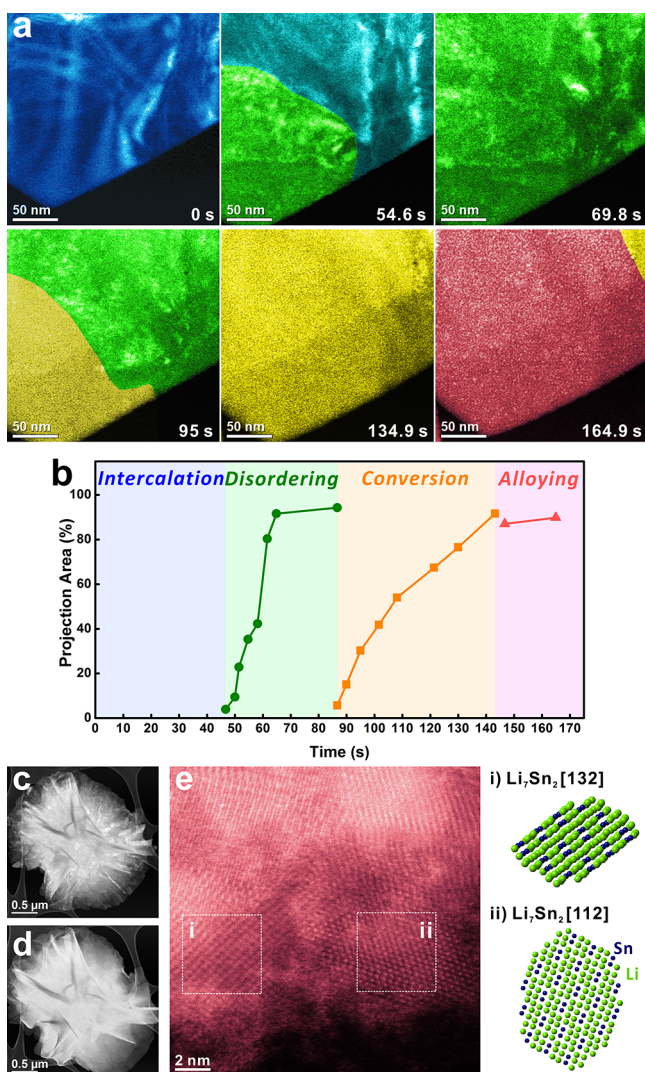

Figure 3. (a) ADF-STEM image series captured in real time. (b) Changes in projection area with different lithiation mechanisms during lithiation. ADF-STEM images acquired from a whole SnS_2 microflower sample (c) before and (d) after lithiation. (e) Atomic resolution HAADF image and atomic models presenting the atomic arrangement of Li_7Sn_2 alloy phase at areas (i) and (ii).

current intensity ($0.3pA/cm^2$) because the relatively stronger electron beam at TEM mode ($14.3 pA/cm^2$) may induce morphological changes of sulfide materials (Figures S8 and S9). We employed a strain-sensitive ADF imaging technique (inner collection angle: 32 mrad) for investigating the multistep lithiation processes of SnS_2, as the phase evolution induces changes in strain at the boundaries.[38,39] While the high-angle ADF signal is determined by average atomic number of the sample, the low-angle ADF signal at 25−50 mrad is very sensitive to the strain field as well as atomic number.[40] Figure 3a presents time-sequence images from an *in situ* ADF-STEM imaging video where false colors indicate different phases. The video was recorded on a single crystalline nanosheet of SnS_2 which was along [001] zone axis. False colors were overlaid on raw ADF-STEM images using Photoshop in order to intuitively visualize the lithiation stages. As particular morphological changes have

been noticed during conversion[38,39] and alloying reactions, we could easily identify the conversion and alloying reactions by *in situ* ADF video. In other words, conversion reaction can be a characteristic indicator for dividing each lithiation step in ADF videos. A movement of phase boundary was observed before the conversion reaction, but after a period time of remaining inactive. Thus, with an assumption of the same lithiation nature of SnS_2, we could resolve four steps of lithium insertion process in the ADF video as intercalation, disordering, conversion, and alloying based on the findings from *in situ* diffraction (Figure 2). Raw video is shown in Movie S2, and raw ADF-STEM images are available in Figure S10. During the initial reaction, we could not see distinct changes in real space video. Since 1.3% of expansion along *a* is too small, we may not detect the possible movement of phase boundary along the observing direction (close to [001]). For the next step, a movement of phase boundary was observed starting at ~45 s, corresponding to the second phase transformation ($Li_xSnS_2 \rightarrow Li_ySnS_2$). In the newly evolved phase, we still observed bend contours indicating the crystalline phase of Li_ySnS_2. The collective structural distortion from 2D layered structure to 3D cubic rock-salt structure contributed to the observed morphological change. Further lithiation induced another phase boundary movement from 85 s, but in this case, bend contours disappeared and fine nanoparticles were formed, which is a typical characteristic of conversion reaction — decomposition of Li_ySnS_2 to Li_2S and Sn. Finally, we observed the localized growth of several nanoparticles, due to the alloying reaction between Sn and Li. But it is difficult to define the nature of Li−Sn alloying reaction since the enlargement of alloying particles happens too quick to be noticed within each nanoparticle. Additional HAADF and HRTEM images after *in situ* lithiation experiments are presented in Figure S11. We plotted the area change of the emerging phases in a function of time for each lithiation step in Figure 3b. Comparing a whole flower-like sample before (Figure 3c) and after lithiation (Figure 3d), there is a recognizable volume expansion, but the original shape was well maintained. In the end, the alloy of Li−Sn formed, and Figure 3e exhibits a high-resolution STEM image after *in situ* lithiation, presenting nanoparticles with [132] and [112] zone-axis of Li_7Sn_2, which is one of Li−Sn alloy compound. Overall, the *in situ* ADF imaging not only provides us fruitful information about phase evolutions in real-space but allows us to see how the morphological changes proceed correlated with phase changes examined by *in situ* electron diffraction.

In order to understand the reaction mechanism and particularly the formation of the disordered rock-salt phase, we performed DFT calculations to investigate the lithiation processes of SnS_2 *via* both equilibrium and nonequilibrium pathways. To explore the equilibrium lithiation reactions, we constructed the Li−Sn−S ternary phase diagram at 0 K by calculating the formation energies of all the known compounds of the Li−Sn−S chemical space from the Inorganic Crystal Structure Database (ICSD).[41] The ground-state reactions of Li-SnS_2 are found to proceed with conversion reactions ($SnS_2 + 2Li \rightarrow SnS + Li_2S$; $SnS_2 + 4Li \rightarrow Sn + 2Li_2S$) and are followed by Sn−Li alloying reactions (Figure S12). Interestingly, both lithium tin disulfides which have been reported: $LiSnS_2$ ($P\bar{3}m1$)[42] and $LiSnS_2$ ($R\bar{3}m$)[43] are predicted to be unstable with positive formation energies according to the DFT phase diagram calculations. Meanwhile, both our observation here and previous reports have shown intercalation steps before conversion reactions during the SnS_2 lithiation.[11,22,27] All these discrepancies suggest that the lithiation of SnS_2 follows a reaction route which deviates

from thermodynamic equilibrium. We therefore simulated non-equilibrium lithiation pathways of SnS_2 using our recently developed nonequilibrium phase searching method as described in Methods.[21,44,45] Starting with all possible Li intercalation sites of the original SnS_2 structure (Figure S13), intermediate phases are identified by exploring a large number of geometrically distinct Li/vacancy configurations on possible insertion sites of the SnS_2 structure at different compositions (Li/vacancy ratios). We find one intermediate phase at $x = 1$ which has a structure reproducing the previously reported $LiSnS_2$ ($P\bar{3}m1$) compound[42] with a formation energy higher than the $LiSnS_2$ ($R\bar{3}m$) compound. In addition, we calculated the cation disordered rock-salt phase (as observed in TEM measurements) using the special quasi-random structure (SQS) method.[46] SQS structures were generated based on a Monte Carlo algorithm as implemented in the Alloy Theoretic Automated Toolkit (ATAT) (Figure S14).[47] Formation energies for all the configurations were then calculated, and the metastable Li-SnS_2 convex hull is constructed from these phases as shown in Figure 4. With energetics from the nonequilibrium intermediate
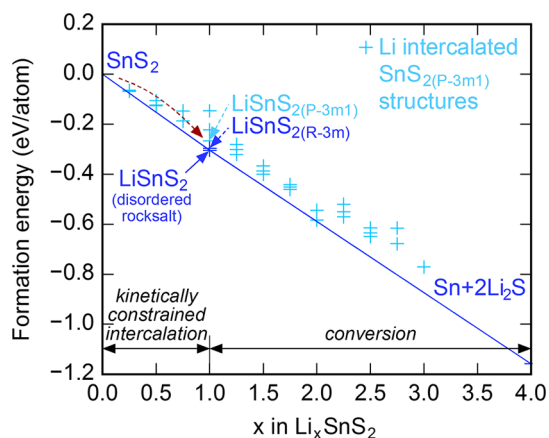

Figure 4. Convex hull generated with the calculated nonequilibrium phases of Li-SnS_2.

phases, the range of computed voltages is in good agreement with the experimental discharge curve as shown in Figure 5. For the composition corresponding to one lithium ion per SnS_2
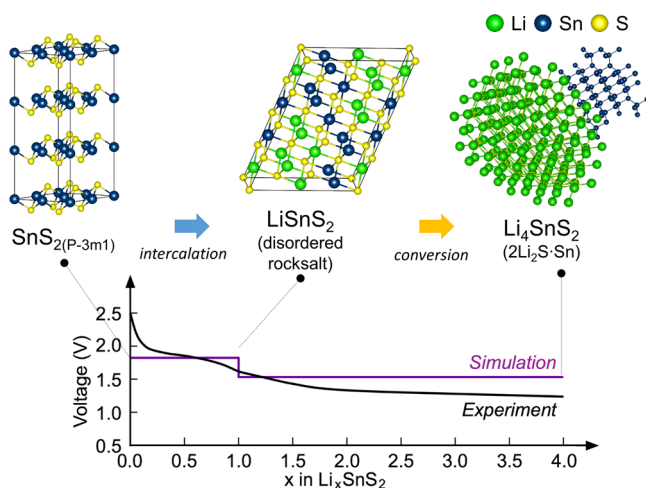

Figure 5. DFT-calculated discharge voltage profile and atomic models corresponding to the predicted intermediate phases during nonequilibrium lithiation process in SnS_2.

inserted ($LiSnS_2$), we find the disordered rock-salt structure is energetically favorable (Figures 4 and 5) by −8 meV/atom compared to the $LiSnS_2$ ($R\bar{3}m$) phase, which is consistent with in situ diffraction results in Figure 2. The disordered rock-salt structure would also be additionally stabilized by entropic contributions. Both the cation disordered structure and the $R\bar{3}m$ structure can be seen as derivatives of the rock-salt structure with different cationic ordering. Considering the extremely small energy difference (8 meV/atom) between those two structures, the energetic impact from the cationic ordering is expected to be limited, and hence entropic contributions stabilize the disordered phase, even at relatively low temperatures. Further lithiation drives a conversion decomposition of Li_xSnS_2 to Li_2S and Sn, which we find as the energetically favorable reaction path (Figures 4 and 5). Calculated potential plateaus at $0 < x < 1$ and $1 < x < 4$ in Figure 4 indicate two-phase transformations from SnS_2 to disordered rock-salt $LiSnS_2$ and from $LiSnS_2$ to Li_2S and Sn, which are consistent with in situ ADF video (Figure 3).

Reversible lithium insertion and extractions of conversion-type electrode are of importance in terms of long-term stability and voltage hysteresis. Understanding the lithium extraction process is crucial for the practical application of conversion-type electrodes. Thus, we performed in situ delithiation experiments. While lithium insertion into electrode materials is thermodynamically spontaneous, pulling out lithium ions from the materials requires a higher potential. In order to provide the potential needed for extracting lithium ions from lithiated SnS_2, we used a Cu mesh grid to directly contact the micron-sized flower sample with Li/Li_2O instead of a lacey film coated grid. The direct touch approach was shown to enable the in situ delithiation process.[27,48,49] After the sample was fully lithiated, we switched the applied voltage from negative (−2 V) to positive (+10 V) to extract lithium ions in lithiated SnS_2. Figure 6a,b presents a radial intensity profile of diffraction patterns, references of Li−Sn alloy phases, Li_2S and metal Sn, and selected time series of diffraction patterns with false colors. Raw video and diffraction patterns are available in Movie S3 and Figure S15. Changes in diffraction patterns during a delithiation are not as dramatic as that occurring during the lithiation (Figure 2), but we could see structural changes, particularly the formation of a metal Sn phase. Figure 6c compares the radial average intensity of diffraction patterns acquired at 0 and 1327 s during lithium extraction, clearly demonstrating the appearance of Sn (220) or (221) peaks. Figure 6d presents the normalized intensity of indicated peaks in Figure 6a in a function of time; ○ indicates Sn (220)/(221), while □,△ originat from Li−Sn alloy phases. Tracking the intensity changes of three peaks with reaction time (Figure 6d) indicates that formation of metal Sn phase takes place at the expense of Li−Sn alloy phase. In our experimental setup for in situ TEM observation, the dealloying process had not been finished, but an ex situ study in Figure 1f demonstrates that charging back to 3 V promotes formation of Sn metals, indicating that conversion reaction of the Li_2S is not reversible and dealloying reaction is the main mechanism of delithiation.

CONCLUSION

In summary, we take advantage of a coupled study of in situ transmission electron microscopy characterization and DFT calculations to elucidate atomistic lithation mechanisms of SnS_2. The in situ electron diffraction provides a high-accuracy measurement of the lattice distortion and reveals a disordering reaction from the 2D layered structure to a cubic disordered
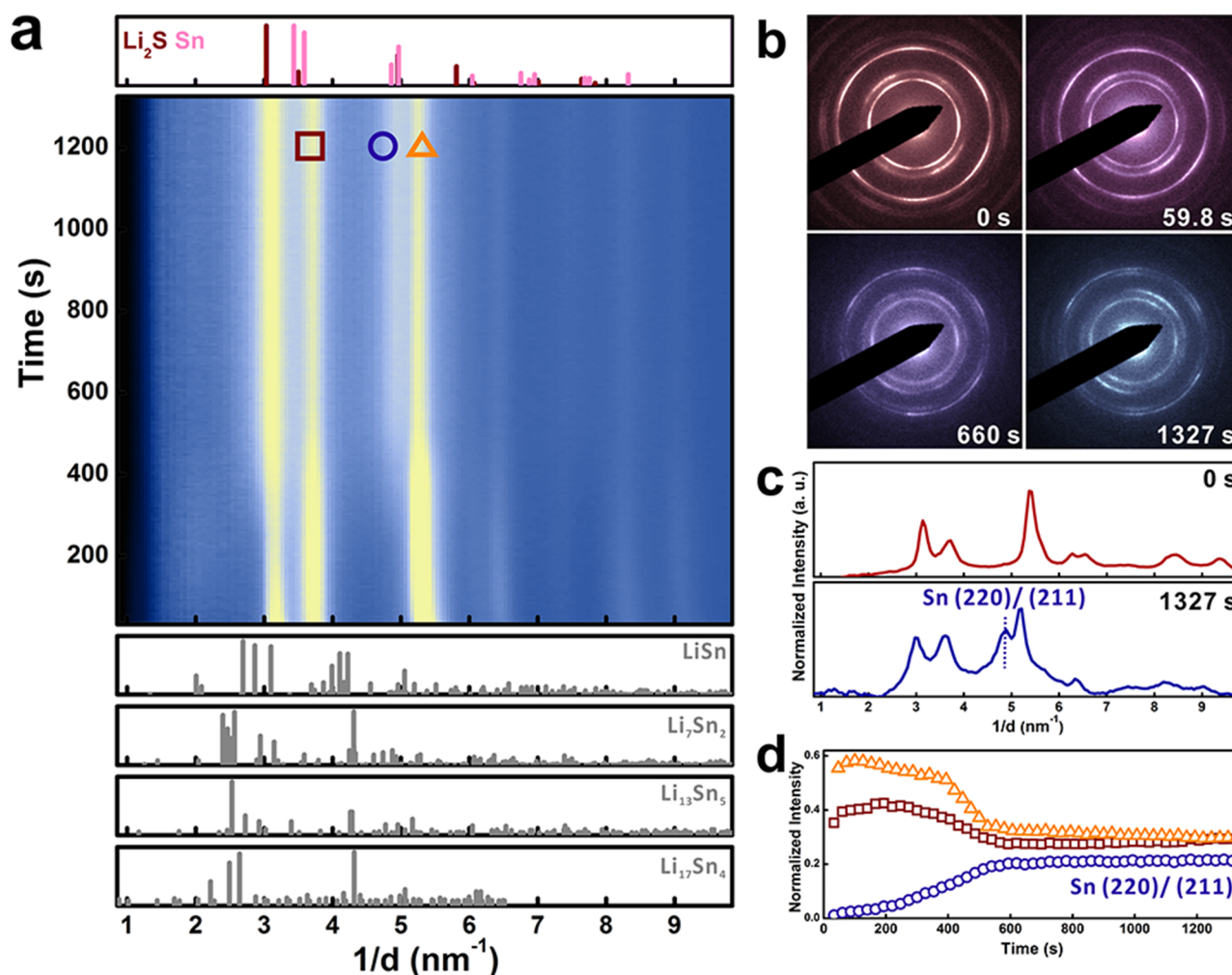
Figure 6. *In situ* SAED patterns of SnS_2 during delithiation. (a) Electron diffraction intensity profile as a function of reaction time during lithium extraction from lithiated SnS_2. Diffraction peaks from the references (Li–Sn alloy phases, Li_2S, and Sn) are also presented. (b) Selected electron diffraction patterns. (c) Radial intensity profiles of diffraction patterns before and after lithium extraction. (d) Intensity profiles of suggested diffraction peaks (□, ○, △ in (a)) with a function of reaction time.

rock-salt structure induced by lithiation. In the rock-salt phase, all the octahedral sites are occupied by cations, restricting the intercalation channels. Further lithiation can only take place *via* a complete decomposition of lithiated compounds to Li_2S and Sn. Our DFT calculations show that the cation disordered rock-salt phase is energetically favorable over the other $LiSnS_2$ phases. Our *in situ* TEM works suggest that the intercalation, disordering, and conversion reactions are two-phase reactions. It is found that the conversion reaction has the slowest reaction speed during lithiation and confirmed the conversion reaction is not reversible during delithiation. The latter one is supposed to be the determining factor to restrict the full usage of SnS_2 for storing Li ions. Combined study of *in situ* TEM and first-principles calculations on the dynamic processes of lithiation here sheds light on revealing reaction mechanisms of 2D electrode materials, which may help to understand their cyclability and stability for alkali secondary batteries.

METHODS

Materials Synthesis. Tetrachlorostannane pentahydrate ($SnCl_4 \cdot 5H_2O$) and 1.2 g thioacetamide (TAA) were dissolved into 40 mL ethanol, and the solution was transferred into a 50 mL Teflon-lined autoclave at 180 °C for 24 h. The SnS_2 precursor were washed repeatedly with deionized water and dried at 60 °C for 8 h.

Electrochemical Measurements. The composite electrode was prepared as a mixed slurry of 80 wt % SnS_2, 10 wt % carbon black, and polyvinylidene fluoride (PvDF) binder in an *N*-methyl pyrrolidone (NMP) solvent. The slurry was casted on a Cu foil which is a current collector. 2032-Type of coin cells were assembled inside an argon-filled glovebox with the as-prepared SnS_2 electrode, Celgard separator, Li metal, and an electrolyte of 1 M lithium hexafluorophosphate ($LiPF_6$) in ethylene carbonate (EC): dimethyl carbonate (DMC) (1:1 in weight). Battery tests were performed on an Arbin BT2000 battery test station with a rate of 50 mA/g.

TEM Characterization. For the post-mortem analysis, Cu TEM grids with SnS_2 sample were incorporated into coin cells with composite electrodes. After a designated potential of 0.01 V (discharged) or 3 V (discharged and charged) had been reached, the coin cells were disassembled, and TEM grids were cleaned with DMC solution inside an argon-filled glovebox. *Ex situ* and *in situ* TEM observations were performed with a JEM-2100F transmission electron microscope (JEOL) at an acceleration voltage of 200 kV. The *in situ* TEM electrochemical cell was incorporated into a Nanofactory TEM-STM specimen holder, where SnS_2 dispersed on a TEM half-grid with lacey carbon support is analogous to active electrode material, current collector, and carbon binders, respectively; Li metal was coated on to a piezo-driven W probe as the counter electrode, and a thin layer of Li_2O formed on Li metal as the solid electrolyte. During lithiation process, a constant negative potential was applied between SnS_2 and Li source, while a constant positive potential was applied for delithiation during

real-time observations. The inner collection angle for ADF imaging is about 32 mrad.

First-Principles Calculations. First-principles density functional theory (DFT) simulations were conducted using Vienna *ab Initio* Simulation Package (VASP)[50,51] with projector augmented wave (PAW) potentials.[52] Generalized gradient approximation (GGA) of Perdew—Becke—Ernzerhof (PBE)[53] was employed with spin polarization for the exchange—correlation functional. The optB86b-vdW functional was also used including a self-consistent van der Waals correction.[54] We used two different sets of parameters: one for sampling lower energy configuration, and the other for determining accurate total energy. For the sampling procedure, kinetic energy cutoff was 300 eV for the plane wave basis set, and Γ-centered grid was approximately 4000 k-point per reciprocal atom. In order for accurate simulation, we expanded calculation ranges: plane-wave basis set cutoff energy of 520 eV and Γ-centered grids with density of 8000 k-points per reciprocal atom.

In order to determine the nonequilibrium phases during Li-SnS$_2$ reaction, the nonequilibrium phase search (NEPS) method was applied.[21,44,45] It was assumed that diffusion rate of Li in SnS$_2$ is much faster than that of Sn or S during lithiation processes. Thus, we expected that Li ions can locate any energetically favorable vacant sites. Detailed procedures of NEPS are as follows: (i) Identify all possible intercalation sites in original structure of SnS$_2$ ($P\bar{3}m1$) using MINT.[55,56] (ii) Figure out all distinctive symmetrical configurations with Enum[57,58] for a series of compositions Li$_x\square_{2-x}$SnS$_2$ ($0 < x < 4$, $\square$: vacancy). (iii) Sample total energies of all the configurations. (iv) For the selected compositions, expected structures were ranked by their total energies, then, three structures having the lowest energy were chosen for further calculation with more strict parameters according to a reaction SnS$_2$ + xLi → Li$_x$SnS$_2$. (v) Build a convex hull using the formation energies. Composition points on the hull were determined as nonequilibrium intermediate phases.

ASSOCIATED CONTENT

Ⓢ Supporting Information

The Supporting Information is available free of charge on the ACS Publications website at DOI: 10.1021/acsnano.8b00758.

> Additional details of pristine materials, raw diffraction patterns and images, data analysis, electron beam effect, DFT calculations (PDF)
> Movie S1 (AVI)
> Movie S2 (AVI)
> Movie S3 (AVI)

AUTHOR INFORMATION

Corresponding Author
*E-mail: dsu@bnl.gov.
ORCID Ⓘ
Zhenpeng Yao: 0000-0001-8286-8257
Kai He: 0000-0003-4666-1800
Liqiang Mai: 0000-0003-4259-7725
Chris Wolverton: 0000-0003-2248-474X
Dong Su: 0000-0002-1921-6683
Notes
The authors declare no competing financial interest.

ACKNOWLEDGMENTS

REFERENCES

(1) Tarascon, J.-M.; Armand, M. Issues and Challenges Facing Rechargeable Lithium Batteries. *Nature* **2001**, *414*, 359−367.

(2) Dunn, B.; Kamath, H.; Tarascon, J.-M. Electrical Energy Storage for the Grid: a Battery of Choices. *Science* **2011**, *334*, 928−935.

(3) Poizot, P.; Laruelle, S.; Grugeon, S.; Dupont, L.; Tarascon, J.-M. Nano-Sized Transition-Metal Oxides as Negative-Electrode Materials for Lithium-Ion Batteries. *Nature* **2000**, *407*, 496−499.

(4) Cabana, J.; Monconduit, L.; Larcher, D.; Palacín, M. R. Beyond Intercalation-Based Li-Ion Batteries: the State of the Art and Challenges of Electrode Materials Reacting Through Conversion Reactions. *Adv. Mater.* **2010**, *22*, E170−E192.

(5) Reddy, M. V.; Subba Rao, G. V.; Chowdari, B. V. R. Metal Oxides and Oxysalts as Anode Materials for Li Ion Batteries. *Chem. Rev.* **2013**, *113*, 5364−5457.

(6) Taberna, P. L.; Mitra, S.; Poizot, P.; Simon, P.; Tarascon, J.-M. High Rate Capabilities Fe$_3$O$_4$-Based Cu Nano-Architectured Electrodes for Lithium-Ion Battery Applications. *Nat. Mater.* **2006**, *5*, 567−573.

(7) Xu, X.; Liu, W.; Kim, Y.; Cho, J. Nanostructured Transition Metal Sulfides for Lithium Ion Batteries: Progress and Challenges. *Nano Today* **2014**, *9*, 604−630.

(8) Badway, F.; Cosandey, F.; Pereira, N.; Amatucci, G. G. Carbon Metal Fluoride Nanocomposites. *J. Electrochem. Soc.* **2003**, *150*, A1318−10.

(9) Zhang, W.-J. A Review of the Electrochemical Performance of Alloy Anodes for Lithium-Ion Batteries. *J. Power Sources* **2011**, *196*, 13−24.

(10) Winter, M.; Besenhard, J. O. Electrochemical Lithiation of Tin and Tin-Based Intermetallics and Composites. *Electrochim. Acta* **1999**, *45*, 31−50.

(11) Morales, J.; Perez-Vicente, C.; Tirado, J. L. Chemical and Electrochemical Lithium Intercalation and Staging in 2H-SnS$_2$. *Solid State Ionics* **1992**, *51*, 133−138.

(12) Balchin, A. A. *Crystallography and Crystal Chemistry of Materials with Layered Structures*; Lévy, F., Ed.; D. Reidel Publishing Company: Dordrecht, 1976; Vol. 2, pp 1−6.

(13) Whittingham, M. S. Electrical Energy Storage Intercalation Chemistry. *Science* **1976**, *192*, 1126−1127.

(14) Whittingham, M. S. Lithium Batteries and Cathode Materials. *Chem. Rev.* **2004**, *104*, 4271−4301.

(15) Lefebvre-Devos, I.; Olivier-Fourcade, J.; Jumas, J. C.; Lavela, P. Lithium Insertion Mechanism in SnS$_2$. *Phys. Rev. B: Condens. Matter Mater. Phys.* **2000**, *61*, 3110−3116.

(16) Stephenson, T.; Li, Z.; Olsen, B.; Mitlin, D. Lithium Ion Battery Applications of Molybdenum Disulfide (MoS$_2$) Nanocomposites. *Energy Environ. Sci.* **2014**, *7*, 209−231.

(17) Benavente, E.; Santa Ana, M. A.; Mendizábal, F.; González, G. Intercalation Chemistry of Molybdenum Disulfide. *Coord. Chem. Rev.* **2002**, *224*, 87−109.

(18) Hwang, H.; Kim, H.; Cho, J. MoS$_2$ Nanoplates Consisting of Disordered Graphene-Like Layers for High Rate Lithium Battery Anode Materials. *Nano Lett.* **2011**, *11*, 4826−4830.

(19) Débart, A.; Dupont, L.; Patrice, R.; Tarascon, J.-M. Reactivity of Transition Metal (Co, Ni, Cu) Sulphides *Versus* Lithium: the Intriguing Case of the Copper Sulphide. *Solid State Sci.* **2006**, *8*, 640−651.

(20) McDowell, M. T.; Lu, Z.; Koski, K. J.; Yu, J. H.; Zheng, G.; Cui, Y. *In Situ* Observation of Divergent Phase Transformations in Individual Sulfide Nanocrystals. *Nano Lett.* **2015**, *15*, 1264−1271.

(21) He, K.; Yao, Z.; Hwang, S.; Li, N.; Sun, K.; Gan, H.; Du, Y.; Zhang, H.; Wolverton, C.; Su, D. Kinetically-Driven Phase Transformation During Lithiation in Copper Sulfide Nanoflakes. *Nano Lett.* **2017**, *17*, 5726−5733.

(22) Kim, T.-J.; Kim, C.; Son, D.; Choi, M.; Park, B. Novel SnS$_2$-Nanosheet Anodes for Lithium-Ion Batteries. *J. Power Sources* **2007**, *167*, 529−535.

(23) Wu, K.; Wu, C. J.; Tseng, C. M.; Chang, J. K.; Lee, T. C. Structure-Mediated Electrochemical Performance of SnS$_2$ Anode for Li-Ion Batteries. *J. Taiwan Inst. Chem. Eng.* **2016**, *66*, 292−300.

(24) Wu, Q.; Jiao, L.; Du, J.; Yang, J.; Guo, L.; Liu, Y.; Wang, Y.; Yuan, H. One-Pot Synthesis of Three-Dimensional SnS$_2$ Hierarchitectures as Anode Material for Lithium-Ion Batteries. *J. Power Sources* **2013**, *239*, 89−93.

(25) Du, Y.; Yin, Z.; Rui, X.; Zeng, Z.; Wu, X.-J.; Liu, J.; Zhu, Y.; Zhu, J.; Huang, X.; Yan, Q.; Zhang, H. A Facile, Relative Green, and Inexpensive Synthetic Approach Toward Large-Scale Production of SnS$_2$ Nanoplates for High-Performance Lithium-Ion Batteries. *Nanoscale* **2013**, *5*, 1456−1459.

(26) Kong, D.; He, H.; Song, Q.; Wang, B.; Yang, Q.-H.; Zhi, L. A Novel SnS$_2$@Graphene Nanocable Network for High-Performance Lithium Storage. *RSC Adv.* **2014**, *4*, 23372−23376.

(27) Gao, P.; Wang, L.; Zhang, Y.-Y.; Huang, Y.; Liao, L.; Sutter, P.; Liu, K.; Yu, D.; Wang, E.-G. High-Resolution Tracking Asymmetric Lithium Insertion and Extraction and Local Structure Ordering in SnS$_2$. *Nano Lett.* **2016**, *16*, 5582−5588.

(28) Yin, K.; Zhang, M.; Hood, Z. D.; Pan, J.; Meng, Y. S.; Chi, M. Self-Assembled Framework Formed During Lithiation of SnS$_2$ Nanoplates Revealed by *in Situ* Electron Microscopy. *Acc. Chem. Res.* **2017**, *50*, 1513−1520.

(29) Su, D.; Wang, F.; Ma, C.; Jiang, N. Engineering Nano-Composite Li$_4$Ti$_5$O$_{12}$ Anodes *via* Scanning Electron-Probe Fabrication. *Nano Energy* **2013**, *2*, 343−350.

(30) Momma, T.; Shiraishi, N.; Yoshizawa, A.; Osaka, T.; Gedanken, A.; Zhu, J.; Sominski, L. SnS$_2$ Anode for Rechargeable Lithium Battery. *J. Power Sources* **2001**, *97−98*, 198−200.

(31) He, K.; Xin, H. L.; Zhao, K.; Yu, X.; Nordlund, D.; Weng, T.-C.; Li, J.; Jiang, Y.; Cadigan, C. A.; Richards, R. M.; Doeff, M.; Yang, X.-Q.; Stach, E. A.; Li, J.; Lin, F.; Su, D. Transitions From Near-Surface to Interior Redox Upon Lithiation in Conversion Electrode Materials. *Nano Lett.* **2015**, *15*, 1437−1444.

(32) Gu, M.; Li, Y.; Li, X.; Hu, S.; Zhang, X.; Xu, W.; Thevuthasan, S.; Baer, D. R.; Zhang, J.-G.; Liu, J.; Wang, C. *In Situ* TEM Study of Lithiation Behavior of Silicon Nanoparticles Attached to and Embedded in a Carbon Matrix. *ACS Nano* **2012**, *6*, 8439−8447.

(33) Nie, A.; Gan, L.-Y.; Cheng, Y.; Asayesh-Ardakani, H.; Li, Q.; Dong, C.; Tao, R.; Mashayek, F.; Wang, H.-T.; Schwingenschlögl, U.; Klie, R. F.; Yassar, R. S. Atomic-Scale Observation of Lithiation Reaction Front in Nanoscale SnO$_2$ Materials. *ACS Nano* **2013**, *7*, 6203−6211.

(34) Shang, T.; Wen, Y.; Xiao, D.; Gu, L.; Hu, Y.-S.; Li, H. Atomic-Scale Monitoring of Electrode Materials in Lithium-Ion Batteries Using *in Situ* Transmission Electron Microscopy. *Adv. Energy Mater.* **2017**, *7*, 1700709−1700716.

(35) Langford, J. I. A Rapid Method for Analysing the Breaths of Diffraction and Spectral Lines Using the Voigt Function. *J. Appl. Crystallogr.* **1978**, *11*, 10−14.

(36) Mecklenburg, M.; Hubbard, W. A.; White, E. R.; Dhall, R.; Cronin, S. B.; Aloni, S.; Regan, B. C. Nanoscale Temperature Mapping in Operating Microelectronic Devices. *Science* **2015**, *347*, 629−632.

(37) Niekiel, F.; Kraschewski, S. M.; Müller, J.; Butz, B.; Spiecker, E. Local Temperature Measurement in TEM by Parallel Beam Electron Diffraction. *Ultramicroscopy* **2017**, *176*, 161−169.

(38) Li, J.; He, K.; Meng, Q.; Li, X.; Zhu, Y.; Hwang, S.; Sun, K.; Gan, H.; Zhu, Y.; Mo, Y.; Stach, E. A.; Su, D. Kinetic Phase Evolution of Spinel Cobalt Oxide During Lithiation. *ACS Nano* **2016**, *10*, 9577−9585.

(39) Hwang, S.; Meng, Q.; Chen, P.-F.; Kisslinger, K.; Cen, J.; Orlov, A.; Zhu, Y.; Stach, E. A.; Chu, Y.-H.; Su, D. Strain Coupling of Conversion-Type Fe$_3$O$_4$ Thin Films for Lithium Ion Batteries. *Angew. Chem., Int. Ed.* **2017**, *56*, 7813−7816.

(40) Muller, D. A.; Nakagawa, N.; Ohtomo, A.; Grazul, J. L.; Hwang, H. Y. Atomic-Scale Imaging of Nanoengineered Oxygen Vacancy Profiles in SrTiO$_3$. *Nature* **2004**, *430*, 657−661.

(41) Belsky, A.; Hellenbrandt, M.; Karen, V. L.; Luksch, P. New Developments in the Inorganic Crystal Structure Database (ICSD): Accessibility in Support of Materials Research and Design. *Acta Crystallogr., Sect. B: Struct. Sci.* **2002**, *58*, 364−369.

(42) Le Blanc, A.; Rouxel, J. Sur Les Types Structuraux Des Composes Intercalaires MSnS$_2$ (M = Li, Na, K, Rb). *C. R. Seances Acad. Sci., Ser. C* **1972**, *274*, 786−788.

(43) Le Blanc, A.; Danot, M.; Rouxel, J. Sur L'insertion De Metaux Alcalins Dans La Structure CdI$_2$ Du Disulfure D'etain. *Bull. Soc. Chim. Fr.* **1969**, *1*, 87−90.

(44) Yao, Z.; Kim, S.; Aykol, M.; Li, Q.; Wu, J.; He, J.; Wolverton, C. Revealing the Conversion Mechanism of Transition Metal Oxide Electrodes During Lithiation From First-Principles. *Chem. Mater.* **2017**, *29*, 9011−9022.

(45) Li, Q.; Yao, Z.; Wu, J.; Mitra, S.; Hao, S.; Sahu, T. S.; Li, Y.; Wolverton, C.; Dravid, V. P. Intermediate Phases in Sodium Intercalation Into MoS$_2$ Nanosheets and Their Implications for Sodium-Ion Batteries. *Nano Energy* **2017**, *38*, 342−349.

(46) Zunger, A.; Wei, S. H.; Ferreira, L. G.; Bernard, J. E. Special Quasirandom Structures. *Phys. Rev. Lett.* **1990**, *65*, 353−356.

(47) van de Walle, A.; Asta, M.; Ceder, G. The Alloy Theoretic Automated Toolkit: a User Guide. *CALPHAD: Comput. Coupling Phase Diagrams Thermochem.* **2002**, *26*, 539−553.

(48) Luo, L.; Wu, J.; Xu, J.; Dravid, V. P. Atomic Resolution Study of Reversible Conversion Reaction in Metal Oxide Electrodes for Lithium-Ion Battery. *ACS Nano* **2014**, *8*, 11560−11566.

(49) Su, Q.; Du, G.; Zhang, J.; Zhong, Y.; Xu, B.; Yang, Y.; Neupane, S.; Kadel, K.; Li, W. *In Situ* Transmission Electron Microscopy Investigation of the Electrochemical Lithiation−Delithiation of Individual Co$_9$S$_8$/Co-Filled Carbon Nanotubes. *ACS Nano* **2013**, *7*, 11379−11387.

(50) Kresse, G.; Hafner, J. *Ab Initio* Molecular Dynamics for Liquid Metals. *Phys. Rev. B: Condens. Matter Mater. Phys.* **1993**, *47*, 558−561.

(51) Kresse, G.; Furthmüller, J. Efficient Iterative Schemes for *Ab Initio* Total-Energy Calculations Using a Plane-Wave Basis Set. *Phys. Rev. B: Condens. Matter Mater. Phys.* **1996**, *54*, 11169−11186.

(52) Blöchl, P. E. Projector Augmented-Wave Method. *Phys. Rev. B: Condens. Matter Mater. Phys.* **1994**, *50*, 17953−17979.

(53) Perdew, J. P.; Ernzerhof, M.; Burke, K. Rationale for Mixing Exact Exchange with Density Functional Approximations. *J. Chem. Phys.* **1996**, *105*, 9982−9985.

(54) Klimeš, J.; Bowler, D. R.; Michaelides, A. Chemical Accuracy for the Van Der Waals Density Functional. *J. Phys.: Condens. Matter* **2010**, *22*, 022201−022206.

(55) Michel, K. J.; Ozoliņš, V. Native Defect Concentrations in NaAlH$_4$ and Na$_3$AlH$_6$. *J. Phys. Chem. C* **2011**, *115*, 21443−21453.

(56) Michel, K. J.; Zhang, Y.; Wolverton, C. Fast Mass Transport Kinetics in B$_{20}$H$_{16}$: a High-Capacity Hydrogen Storage Material. *J. Phys. Chem. C* **2013**, *117*, 19295−19301.

(57) Hart, G. L. W.; Forcade, R. W. Algorithm for Generating Derivative Structures. *Phys. Rev. B: Condens. Matter Mater. Phys.* **2008**, *77*, 34−12.

(58) Hart, G. L. W.; Forcade, R. W. Generating Derivative Structures From Multilattices: Algorithm and Application to Hcp Alloys. *Phys. Rev. B: Condens. Matter Mater. Phys.* **2009**, *80*, 014120−014128.